Analysis of errors in corneal topography evaluation caused by distortion aberration in the camera lens of a cone corneal topographer

O. Huerta-Carranza

Departamento de Física, Facultad de Ciencias, Universidad Nacional Autónoma de Mexico, Ciudad Universitaria, Ciudad de México, 04510, Mexico.

F. Granados-Agustín

Instituto Nacional de Astrofísica, Óptica y Electrónica, Apartado Postal 216, 72000, Puebla, Pue., México.

J. Ocampo-López-Escalera

Department of Health, El Colegio de La Frontera Sur, San Cristóbal de Las Casas, 29290 Chiapas, Mexico.

M. Campos-García and M. Avendaño-Alejo

Instituto de Ciencias Aplicadas y Tecnología, Universidad Nacional Autónoma de México, Circuito Exterior S/N, Ciudad Universitaria, 04510, México City.

Received 1 October 2024; accepted 23 April 2025

We study the effects on corneal topography when the topographer camera is affected by distortion aberration, causing a nonuniform magnification in the image recorded by the camera sensor. As a result, images present a size change which could mislead the interpretation of the vertex position of the anterior corneal surface. Images numerically generated and distorted using the Seidel's aberrations are used to carry out the analysis. According to the results presented in this paper, while the reconstruction algorithm accurately recovers the central region of the surface, there are pronounced deviations between the retrieved surface and the actual surface towards the periphery. These deviations could lead to the underestimation or overestimation of the parameters associated with the base surface for a contact lens, affecting the correction of refractive errors such as myopia, hyperopia or astigmatism. Moreover, if the corneal topography provided by a topographer affected by distortion aberration is used for corneal reshaping via laser ablation, the refractive errors might be overcorrected or undercorrected. Thus, this paper highlights the importance of performing a proper calibration procedure for the distortion aberration of the corneal topographer camera, in order to reliably recover an accurate corneal topography.

Keywords: Corneal topography; null test; geometrical optics.

DOI: https://doi.org/10.31349/RevMexFis.71.051305

1. Introduction

The cornea is the first optical element of the human eye to interact with incident light, providing about two-thirds of the eye's refractive power. The majority of this bending occuring at the air-cornea interface [1]. Two of the primary visual disorders affecting humans, astigmatism and keratoconus, occur in the anterior surface of this transparent tissue. Astigmatism, characterized by a degraded image on the retina, results from the lack of revolution symmetry of the anterior corneal surface. In contrast, keratoconus is caused by a progressive corneal thinning and protrusion, resulting in an uneven distribution of refractive power and blurred image at the retina [2]. For analyzing these visual defects, the corneal surface can be modeled as a sphero-torical or biconical surface in the first case and a freeform surface in the second case. The effects of astigmatism and keratoconus on vision can be reduced through the use of spectacles or contact lenses [3]. In certain cases, corneal refractive surgery may be a viable option [4–6]. However, it is essential to accurately determine the shape of the cornea in order to perform an appropriate fitting of ophthalmic lenses or to reshape the corneal surface through refractive surgery.

Corneal topographers are the standard ophthalmic instruments utilized for the evaluation of the anterior corneal surface. These instruments are traditionally based on Placido's disc, consisting of a collection of alternating dark and bright rings placed inside a concave surface [7–9]. At the center of this surface, a camera is positioned in order to observe the projection of the rings onto the corneal surface. Calibration of the corneal topographer is crucial for obtaining an accurate representation of the anterior corneal surface topography. There are two principal stages comprising the calibration procedure. First, the position and orientation of the bright rings must be computed on the concave surface in relation to the camera sensor or detection plane. The second step addresses to the distortion aberration introduced by the camera lens used to record the images, in order to evaluate the corneal surface. The camera of the corneal topographer consists of a set of lenses with a diaphragm, which can be closed

to its minimum aperture to reduce the effects of optical aberrations on the image. However, the distortion aberration still affects the image formed on the detection plane [10]. The distortion aberration does not degrade the image quality, but it causes radial displacements of image points with respect to the optical axis of the camera lens. This is due to a nonuniform magnification produced by the camera lens. Therefore, a calibration procedure must be implemented to reduce the effects of the distortion aberration on the image recorded by the camera sensor [11, 12].

In this work, we present a numerical simulation analysis of how distortion aberration in the camera lens of the corneal topographer affects the assessment of the corneal topography measurements. In previously published works [13–15], we proposed an inexpensive and portable corneal topographer, consisting of a smartphone and a truncated cone. We have designed this particular device based on the Null Screen Method (NSM), which considers an exact ray tracing to design a set of elongated ellipses displayed along the truncated cone denoted as the target or null-screen. Ideally, we assume that the anterior corneal surface of the eye works as a convex spherical mirror, reflecting the target projected onto it. The reflected light is then collected by a positive lens and focused onto the detection plane, resulting in an image consisting of an array of bright spots. When the test surface matches the average corneal shape, a regular pattern of bright spots is projected onto the detection plane. Any deviation from this ideal pattern indicates deviations or misalignments of the test surface from the actual corneal surface. Utilizing a spots pattern instead of a ringed one ensures a one-to-one correspondence between the target and the image points, even for surfaces that are not rotationally symmetric avoiding the skew ray error [16–19].

Using numerical simulations, the synthetic image without distortion that would be expected to be recorded on the camera sensor, taking into account that the test surface corresponds to a biconical surface, was computed. Third-order Seidel's aberrations theory [20] was used to model the radial distortion aberration in the synthetic image, while other optical aberrations were neglected. The distortion aberration can manifest as a barrel distortion (positive) or as a pincushion distortion (negative). In the first case, off-axis image points displace inward with respect to the undistorted image, while in the second case they displace outward. In practice, these changes in image size might be wrongly interpreted as displacements of the corneal surface along the instrument optical axis or deviations of paraxial radius of curvature with respect to the true value. In addition, our results indicated that when the corneal surface is affected by astigmatism and the camera lens exhibits distortion aberration, the classical hourglass or bow-tie pattern that appears in the axial and tangential maps [21] does not change its orientation, provided that the cornea is aligned with the instrument axis. This conclusion is obtained by applying a range of distortion values, ranging from negative to positive. Each distorted image is ideally considered as if it was obtained from the corneal topographer, allowing us to retrieve the corneal topography and compare it to the actual corneal topography.

The present paper is structured as follows. Section 2 presents a detailed description of the exact ray tracing methodology employed in the design of the object pattern or target, which is positioned within a truncated cone. Section 3 outlines the calculation of synthetic images on the sensor plane when the surface under study deviates from the average corneal surface. Section 4 describes the reconstruction method and illustrates the process to calculate the sagittal and tangential maps of refractive power. Section 5 presents the results corresponding to the numerical simulations. Finally, Sec. 6 summarizes our conclusions based on the obtained results.

2. Corneal topographer

In a previously published work [14], we propose a corneal topographer that basically consists of a commercial smartphone and a truncated cone, as depicted in Fig. 1. A set of bright objects are designed inside the truncated cone and projected onto the cornea. The reflected rays are collected by the smartphone camera lens and recorded on the detection plane (**DP**). A backward ray tracing is used to design the target inside a truncated cone, *i.e.*, the ray tracing starts in the detection plane and ends on the truncated cone, allowing us to choose the image that should form on the detection plane when the surface has certain previously defined characteristics.

2.1. The ideal image design

As a starting point for designing the target, an array of small circles was selected as the ideal image. The distribution of the circles on the detection plane corresponds to a quasi-radial array, *i.e.*, a set of small circles is distributed on concentric rings, as shown in Fig. 2a), whose area is limited by the active region of the sensor, and the size of the circumferences is restricted to maximum resolution of pixels associated to different commercial smartphones. The ideal image is presented in a square domain $[-0.5$ mm, 0.5 mm$]\times[-0.5$ mm, 0.5 mm], as shown in Fig. 2a).

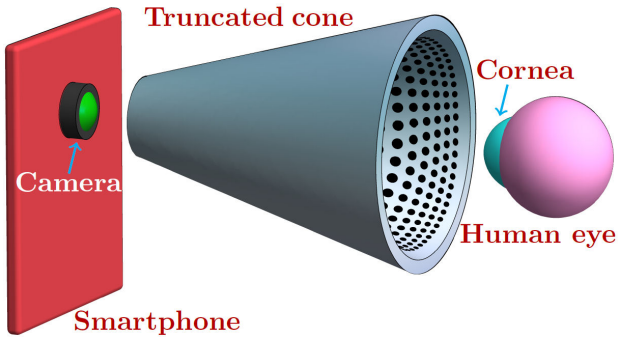

FIGURE 1. Schematic diagram of the corneal topographer design used for the numerical analysis.

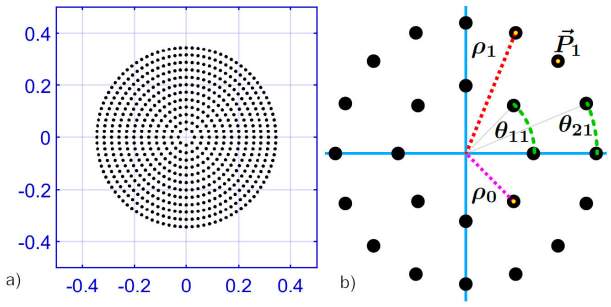

FIGURE 2. a) Ideal image used to design the target. b) Close-up of the first two rings of the ideal image.

The number of circles per ring increases proportionally with the radius of each ring. The Cartesian coordinates $\vec{P}_1{=}(x_1, y_1)$ of the circle centers in the image are given by

$$x_1 = \rho_i \cos(\theta_{ij}), \quad y_1 = \rho_i \cos(\theta_{ij}), \tag{1}$$

where subscripts i and j make references to the radial coordinate and the azimuthal angle, respectively. In Eq. (1), the polar coordinates (ρ_i, θ_{ij}) can be written as

$$\rho_i{=}\rho_0 + (i-1)\left(\frac{\rho_N - \rho_0}{N}\right), \quad 1 \leq i \leq N+1, \tag{2a}$$

$$\theta_{ij}{=}\left[\frac{2\pi}{\eta_0 + (i-1)\eta}\right] j, \quad 0 \leq j < \eta_0 + (i-1)\eta, \tag{2b}$$

the quantities i, j, N, η_0 and η are integer numbers. $N+1$ is the number of rings. η_0 is the number of circles on the first ring ($i{=}1$). η is the increase in the number of circles between two consecutive rings. The number of circles on the i-th ring is given by $\eta_0 + (i-1)\eta$. The radii corresponding to the first and last rings are ρ_0 and ρ_N, respectively. In Table I, we listed the values of each parameter that appear in Eq. (2a) and Eq. (2b). Figures 2a) shows the ideal image used to design the target or null-screen, with axes scaled in millimeters. Additionally, Fig. 2b) shows a close-up of the first two rings.

2.2. Exact equations for the backward ray tracing

A schematic representation of the corneal topographer, in the **YZ** plane, is depicted in Fig. 3. Each ray is traced considering the pinhole camera model without taking into account the lens distortion; therefore, all the rays pass through the camera pinhole without deviation.

TABLE I. Parameters used for designing the ideal image.

Parameter	Value
ρ_0 (μm)	31
ρ_N (mm)	0.35
N	11
η_0	8
η	8

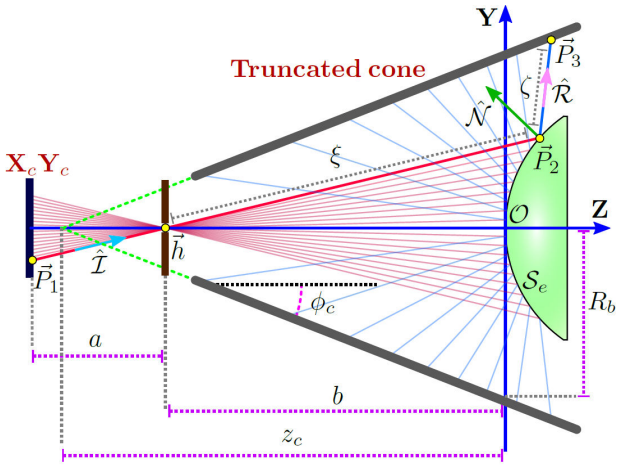

FIGURE 3. Schematic diagram of ray tracing used in the design of the target or null-screen.

The ray tracing starts at a point $\vec{P}_1{=}(x_1, y_1, -a-b)$ on the detection plane, which is denoted by $\mathbf{X}_c\mathbf{Y}_c$. The quantity a is the separation between the $\mathbf{X}_c\mathbf{Y}_c$ plane and the pinhole situated at $\vec{h}{=}(0,0,-b)$ and b is the spacing between the pinhole position and the vertex of the reflecting surface $\mathcal{S}_e$, which is representing the anterior corneal surface. a and b are defined along the **Z**-axis, as schematized in Fig. 3. The unit vector $\hat{\mathcal{I}}{=}(\mathcal{I}_x, \mathcal{I}_y, \mathcal{I}_z)$ denotes the direction of the incident ray that passes through the pinhole and is propagated up to strike the reflecting spherical surface ($\mathcal{S}_e$) at $\vec{P}_2$, as shown in Fig. 3. An expression for $\hat{\mathcal{I}}$ can written as follows

$$\mathcal{I} = \frac{(-x_1, -y_1, a)}{\sqrt{x_1^2 + y_1^2 + a^2}}, \tag{3}$$

where $\mathcal{S}_e$ is proposed to be a spherical surface aligned with the corneal topographer axis with its vertex located at the Origin of the coordinates denoted by $\mathcal{O}$, as depicted in Fig. 3. The analytical expression for $\mathcal{S}_e$ is given by

$$S_e(x, y, z) = \rho^2 - 2r_e z + z^2, \tag{4}$$

where $\rho = (x^2 + y^2)$ and r_e is the radius of curvature corresponding to the average spherical cornea. The rays after being reflected by $\mathcal{S}_e$ hit the truncated cone at $\vec{P}_3$. From Fig. 3, the propagation distance ξ of the incident ray from $\vec{h}$ to $\vec{P}_2$ can be calculated using the following expression

$$\xi = \left(-B - \sqrt{B^2 - AC}\right)/A, \tag{5}$$

the parameters A, B and C can be obtained in terms of $\hat{\mathcal{I}}$, $\vec{h}$ and r_e, as follows

$$A = 1, \tag{6a}$$

$$B = \mathcal{I}_z(b - r_e), \tag{6b}$$

$$C = b^2 - 2r_e b. \tag{6c}$$

Considering the value for ξ, the point $\vec{P}_2$ can be obtained using the following vector equation of a straight line

$$\vec{P}_2 = \vec{h} + \xi\hat{\mathcal{I}}. \tag{7}$$

Once $\vec{P}_2$ is determined, we calculate the direction of the reflected ray, denoted by the unit vector $\hat{\mathcal{R}}=(\mathcal{R}_x, \mathcal{R}_y, \mathcal{R}_z)$. Using the vector law of the reflection $\hat{\mathcal{R}}$ is given by

$$\hat{\mathcal{R}} = \hat{\mathcal{I}} - 2\left(\hat{\mathcal{I}} \cdot \hat{\mathcal{N}}\right)\hat{\mathcal{N}}, \tag{8}$$

the unit vector $\hat{\mathcal{N}}$ is the direction of the normal vector at $\vec{P}_2$. $\hat{\mathcal{N}}$ can be obtained from the gradient of Eq. (4). Using Eq. (7) and (8), a point $\vec{P}_3 = (x_3, y_3, z_3)$ on the truncated cone can be written as

$$\vec{P}_3 = \vec{P}_2 + \zeta\hat{\mathcal{R}}, \tag{9}$$

where ζ is defined as the propagation distance of the reflected ray from $\vec{P}_2$ to $\vec{P}_3$. The truncated cone is represented by means of the following expression

$$z_3 = \tan\left(\frac{\pi}{2} - \phi_c\right)\rho_3 + z_c, \tag{10}$$

where z_c is the axial position of the cone vertex along the **Z**-axis, $\rho_3 = \sqrt{x_3^2 + y_3^2}$ and ϕ_c is called the semi-vertical angle of the cone (see Fig. 3). For obtaining the Cartesian coordinates of $\vec{P}_3$, we substitute Eq. (9) into Eq. (10). As a result an equation of the second degree in ζ is obtained. Its solution has the same structure as the one obtained for ξ in Eq. (5), with the modification that A, B, and C are replaced by A', B' and C', which are given as follows:

$$A' = (\tan\phi_m)^2\left(\mathcal{R}_x^2 + \mathcal{R}_y^2\right) - \mathcal{R}_z^2, \tag{11a}$$

$$B' = \left[(z_c - z_2)\,\mathcal{R}_z + (\tan\phi_m)^2\left(x_2\mathcal{R}_x + y_2\mathcal{R}_y\right)\right], \tag{11b}$$

$$C' = (\tan\phi_m)^2\left(x_2^2 + y_2^2\right) - (z_2 - z_c)^2, \tag{11c}$$

where $\phi_m{=}(\pi/2 - \phi_c)$. Substituting Eqs. (11a)-(11c) into Eq. (5), the value for ζ can be calculated and the intersection point $\vec{P}_3$ can be determined from Eq. (9). Taking into account the ideal image designed in Sec. 2.1 [see Fig. 2a)] and the equations deduced throughout this section, we can design the object pattern inside the truncated cone. The separation between the pinhole and the $\mathbf{X}_c\mathbf{Y}_c$ plane (detection plane) is $a = 5.2$ mm. The distance between the vertex of the surface $\mathcal{S}_e$ and the pinhole is $b = 70$ mm. The radius of the cone in the $\mathbf{XY}$ plane is denoted by R_b, as shown in Fig. 3. The radius of curvature of the reflecting spherical surface $\mathcal{S}_e$ is $r_e = 7.8$ mm, its height map is plotted in a square domain

TABLE II. Null-screen method parameters for designing the target in the truncated cone.

Spherical surface		Truncated cone	
Parameter	Value	Parameter	Value
r_e (mm)	7.8	ϕ_c (°)	10.79
a (mm)	5.2	R_b (mm)	16
b (mm)	70	z_c (mm)	85.5

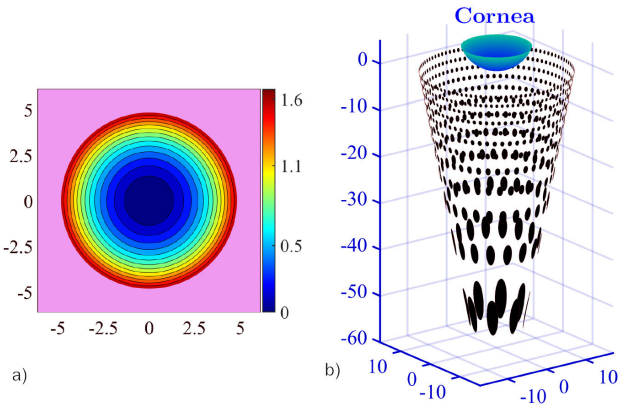

FIGURE 4. a) Height map for the spherical surface $\mathcal{S}_e$. b) Structure of the pattern consisting of a set of elongated ellipses.

TABLE III. Parameters of the biconical surface under study.

Parameter	Value
r_x (mm)	8.35
r_y (mm)	7.63
k_x	-0.43
k_y	-0.25
α (°)	17

domain [−6.1 mm, 6.1 mm]×[−6.1 mm,6.1 mm], as shown in Fig. 4a). Applying the Null-Screen Method using the values listed in Table II, we obtain a set of elongated ellipses which are designed inside the truncated cone, as shown in Fig. 4b). We must highlight that an advantage of the NSM is its capacity to identify misalignments or deformations of the surface under test after a qualitative inspection of the image recorded on the sensor camera.

3. Synthetic images

Throughout this section, we show how to calculate the synthetic images on the detection plane when the anterior corneal surface under study does not coincide with the spherical surface $\mathcal{S}_e$. We assume that the corneal surface under test can be modeled as a biconical surface, whose analytical expression S is given by

$$\mathcal{S} = \frac{c_x(x_r - x_0)^2 + c_y(y_r - y_0)^2}{1 + \sqrt{1 - Q_x c_x^2(x_r - x_0)^2 - Q_y c_y^2(y_r - y_0)^2}}, \tag{12}$$

the vertex of the biconical surface coincides with the origin of coordinates $\mathcal{O}$. $r_x{=}1/c_x$ and $r_y{=}1/c_y$ are the radii of curvature along the x and y axes, respectively. $Q_x{=}1 + k_x$ and $Q_y{=}1 + k_y$, where k_x and k_y are the conic constants along the x and y axes, respectively. Furthermore, we suppose that the biconical surface $\mathcal{S}$ is rotated by the angle α about the

Z-axis; therefore, the Cartesian coordinates x_r and y_r, that appear in Eq. (12), can be written in the following form

$$x_r = x\cos\alpha - y\sin\alpha, \tag{13a}$$

$$y_r = x\sin\alpha + y\cos\alpha. \tag{13b}$$

The ideal values corresponding to the parameters involved in Eqs. (12), (13a) and (13b) are listed in Table III.

3.1. Calculating of synthetic images

In this section, we show how to calculate the synthetic images that should be recorded on the camera sensor. In practice, the biconical surface must be placed in front of the truncated cone, as illustrated in Fig. 1 and Fig. 3. As a result, a set of bright spots forms on the detection plane, their positions are denoted by $(x_1, y_1, -a-b)$. According to the scheme shown in Fig. 3, the ray starts at $\vec{P}_3$ and passes through $\vec{h}$, the unknown is the point $\vec{P}_2$ on the biconical surface. The normal vector at $P_2{=}(x, y, \mathcal{S}(x, y))$ must satisfy the vector law of reflection (see Eq. (8)). The unit vectors $\hat{\mathcal{I}}$, $\hat{\mathcal{R}}$ and $\hat{\mathcal{N}}$, involved in Eq. (8), can be conveniently written as

$$\hat{\mathcal{I}} = \frac{\vec{P}_2 - \vec{h}}{\left(\parallel \vec{P}_2 - \vec{h} \parallel\right)}, \tag{14a}$$

$$\hat{\mathcal{R}} = \frac{\vec{P}_3 - \vec{P}_2}{\left(\parallel \vec{P}_3 - \vec{P}_2 \parallel\right)}, \tag{14b}$$

$$\hat{\mathcal{N}} = \frac{(-\mathcal{S}_x, -\mathcal{S}_y, 1)}{\left(\mathcal{S}_x^2 + \mathcal{S}_y^2 + 1\right)^{1/2}}, \tag{14c}$$

where $\mathcal{S}_x$ and $\mathcal{S}_y$ are the partial derivatives of $\mathcal{S}(x, y)$ with respect to x and y, respectively. Taking into account Eq. (8) and after some algebraic manipulations, the Cartesian components of $\hat{\mathcal{I}}$, $\hat{\mathcal{R}}$ and $\hat{\mathcal{N}}$ satisfy the following expressions [22,23]

$$(\mathcal{R}_x - \mathcal{I}_x) + (\mathcal{R}_z - \mathcal{I}_z)\,\mathcal{S}_x = 0, \tag{15a}$$

$$(\mathcal{R}_y - \mathcal{I}_y) + (\mathcal{R}_z - \mathcal{I}_z)\,\mathcal{S}_y = 0. \tag{15b}$$

Eqs. (15a) and (15b) form a system of two nonlinear equations in two unknowns x and y. This system of equations can be solved in numerical form using the Levenberg-Marquardt algorithm, which is implemented in the MATLAB toolbox. Once this system of equations is solved, the incident point $P_2{=}(x, y, \mathcal{S}(x, y))$ can be known. Therefore, the direction $\hat{\mathcal{I}}$ can be calculated by means of Eq. (14a). Calculating the intersection between the prolongation of the ray and the detection plane (see Fig. 3), the Cartesian coordinates of the image points $\vec{P}_1{=}(x_1, y_1, z_1)$ can be obtained as

$$x_1 = -a\,(\mathcal{I}_x/\mathcal{I}_z)\,;\; y_1 = -a\,(\mathcal{I}_y/\mathcal{I}_z)\,;\; z_1 = -a-b. \tag{16}$$

Figure 5a) shows a height map corresponding to the biconical surface or corneal surface under test. Figure 5b) shows the image obtained from Eq. (16), that must form on the detection plane when the surface under study corresponds to the biconical surface given by Eq. (12) and Table III. Once more, the synthetic image is treated as if it had been experimentally obtained from the corneal topographer, as seen below. Additionally, Fig. 5d) shows the undistorted chequerboard image, which will be used to qualitatively demonstrate distortion effects. The dimensions of the checker board image are 0.8×0.8 mm^2.

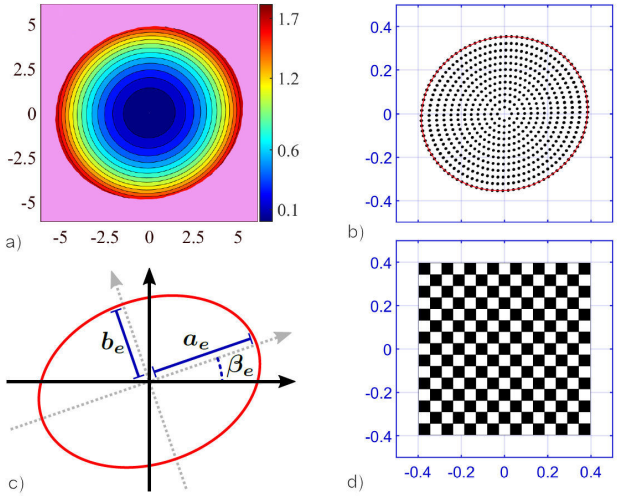

FIGURE 5. a) Height map for the corneal surface under test modeled as a biconical surface. b) Simulated synthetic image formed on the detection plane, assuming the test surface is a biconical surface. c) Parameters of the elliptical contour that encloses the image points. d) Undistorted image of a checkerboard.

Using the algorithm described in Ref. [24], the dots in the image [see Fig. 5b)] can be enclosed by an ellipse, the equation of which is as follows

$$\begin{pmatrix} x_e \\ y_e \end{pmatrix} = \begin{pmatrix} \cos\beta_e & -\sin\beta_e \\ \sin\beta_e & \cos\beta_e \end{pmatrix} \begin{pmatrix} a_e\cos\phi_e \\ b_e\sin\phi_e \end{pmatrix}, \tag{17}$$

where $\beta_e{=}17.0°$ is the angle of rotation corresponding to the elliptical contour, $a_e{=}0.3876$ mm and $b_e{=}0.3507$ mm are the semi-major and the semi-minor axes of the ellipse, respectively, as illustrated in Fig. 5c)]. ϕ_e is the polar angle in the polar coordinates. This ellipse is used in the next section for quantifying the change in size of the images affected by several degrees of distortion aberration. In this case, the area of the elliptical contour is $A_e = 0.4270$ mm^2.

3.2. Synthetic images affected by the distortion aberration

As mentioned in Sec. 2, the ray tracing performed to obtain the target and the synthetic images utilizes the pinhole camera model, which does not take into account the distortion aberration associated with the camera lens [25]. However, in practice, even when other aberrations are corrected, distortion aberration is always present in the optical system and must be calibrated. The aim of this section is to obtain images

affected by distortion aberration and to recover the corneal topography assuming that the distorted images were experimentally obtained. We propose to model the distortion aberration using the Seidel's Aberrations; therefore, the Cartesian coordinates (x_d, y_d) affected by distortion aberration can be conveniently written as [10]

$$x_d = x_1 + \left(\frac{\sigma}{M_T^3}\right)\left(x_1^2 + y_1^2\right) x_1, \tag{18a}$$

$$y_d = y_1 + \left(\frac{\sigma}{M_T^3}\right)\left(x_1^2 + y_1^2\right) y_1, \tag{18b}$$

where M_T and σ are the transversal magnification and the distortion coefficient, correspondingly. When σ=0, (x_d, y_d) corresponds to the Cartesian coordinates (x_1, y_1) of the image without distortion, which is shown in Fig. 5b). For the sake of simplicity, in Eqs. (18a) and (18b) we have only considered radial distortion; however, a more realistic model for the distortion aberration must also take into account the tangential distortion [26, 27].

For obtaining some images affected by radial distortion aberration, we assign values to σ which range from negative values to positive values. Tested values for σ are tabulated in Table IV. The value for the transversal magnification M_T was extracted from a previously published work by the authors in Ref. [14], the minus sign of M_T implies that the image recorded on the camera sensor was inverted.

On the one hand, Figs. 6a)-6c) show three images affected by negative distortion also called pincushion distortion. On the other hand, Figs. 6d)-6f) show three images affected by positive distortion also known as barrel distortion. The images are shown in a square domain [-0.5 mm, 0.5 mm]×[-0.5 mm, 0.5 mm]. The image without distortion corresponding to the distortion coefficient $\sigma_4 = 0$ is the synthetic image shown in Fig. 5b). The value of σ increases from Fig. 6a) to Figs. 6f) and the dimensions corresponding to the elliptical contour that encloses the dots diminishes from Fig. 6a) to 6f). The above effects can be easily appreciated from the deformed checkerboards. By fitting Eq. (17) to the boundary points in Figs. 6a) - 6f), using the algorithm described in Ref. [24], the parameters defining each elliptical contour can be obtained. These parameters are listed in Table V. The parameter $\mathcal{E}_A$ shown in Table V, the percentage increase or decrease in area for each elliptical contour. A negative value for $\mathcal{E}_A$ signifies a decrease in area.

Before the corneal examination can be performed, either ophthalmologist or optometrist should align the human cornea with the instrument for obtaining a focused image on the camera sensor. From the change in size of the images shown in Figs. 6a)-6e), when the camera lens suffers from distortion aberration in accordance with Table V, we can be tempted to assume that the surface under test is displaced with respect to the Origin of coordinates $\mathcal{O}$, along the optical axis of the corneal topographer. Another possible assumption for the change in image size is that the paraxial radius of curvature of the surface under test deviates from the average cornea curvature whose vertex should be at $\mathcal{O}$. Both assumptions may lead to inaccurate results in corneal topography assessment, which will be addressed in the following sections.

TABLE IV. Tested values for the distortion coefficients and transversal magnification.

Parameter	Value	Parameter	Value
σ_1 (mm^{-2})	-2.0×10^{-4}	σ_5 (mm^{-2})	1.41×10^{-6}
σ_2 (mm^{-2})	-6.3×10^{-5}	σ_6 (mm^{-2})	6.3×10^{-5}
σ_3 (mm^{-2})	-1.41×10^{-6}	σ_7 (mm^{-2})	2.0×10^{-4}
σ_4 (mm^{-2})	0	M_T	-0.065

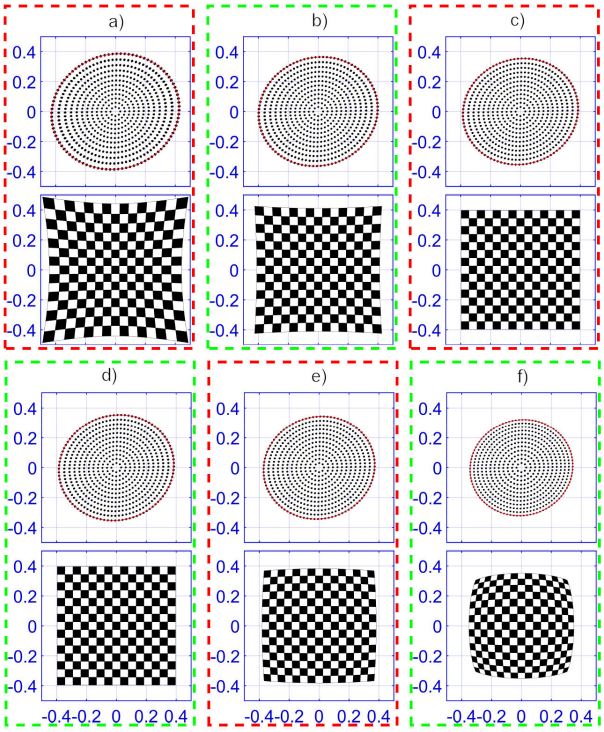

FIGURE 6. Images affected by pincushion distortion: a) $\sigma_1 = -2.0 \times 10^{-4}$, b) $\sigma_2 = -6.3 \times 10^{-5}$ and c) $\sigma_3 = -1.41 \times 10^{-6}$. Images affected by barrel distortion: d) $\sigma_5 = 1.41 \times 10^{-6}$, e) $\sigma_6 = 6.3 \times 10^{-5}$ and f) $\sigma_7 = 2.0 \times 10^{-4}$. In all cases, the axes units are expressed in mm.

TABLE V. Parameters corresponding to each elliptical contour plotted in Figs. 6a)-6f).

Fig.	$[a_e\ , b_e]$ (mm)	β_e (°)	Area (mm^2)	$\mathcal{E}_A$ (%)
6a)	[0.4301, 0.3821]	17.0001	0.5163	20.89
6b)	[0.4010, 0.3606]	17.0000	0.4542	6.36
6c)	[0.3879, 0.3509]	17.0000	0.4276	0.14
6d)	[0.3873,0.3505]	17.0000	0.4264	-0.14
6e)	[0.3743, 0.3408]	17.0000	0.4007	-6.16
6f)	[0.3452, 0.3193]	17.0003	0.3463	-18.90

4. Method for recovering the corneal topography

In this section, we will briefly describe the implementation of a numerical method to recover the corneal topography of the anterior corneal surface, based on the Zonal and Modal reconstructions proposed by the authors in Ref. [23]. Furthermore, we show how to calculate the axial and tangential powers corresponding to the recovered surface.

4.1. The shape retrieving of the surface under test

The reconstruction algorithm takes as input the direction $\hat{n}=(n_x, n_y, n_z)$ of the normal vectors to the surface under test. $\hat{n}$ can be written in terms of the directions of the reflected and incident rays as follows

$$\hat{n} = \frac{\left(\hat{\mathcal{R}} - \hat{\mathcal{I}}\right)}{\left(\parallel \hat{\mathcal{R}} - \hat{\mathcal{I}} \parallel\right)}, \tag{19}$$

in practice, only the direction $\hat{\mathcal{I}}$ of the incident ray can be determined by means of Eq. (3). However, in accordance with Eq. (14b), the reflected ray cannot be obtained because the incidence point $\vec{P}_2$ is unknown. However, $\vec{P}_2$ can be approximated by the intersection point $\vec{P}_2'$ between the ray and a surface represented by $\mathcal{G}(x, y)$, as depicted in Fig. 7.

We propose that $\mathcal{G}(x, y)$ coincides with the spherical surface $\mathcal{S}_e$ that was considered to design the null-screen in Sec. 2. The intersection point $\vec{P}_2'$ can be calculated using Eq. (5) and Eq. (7). Substituting $\vec{P}_2'$ into Eq. (14b), the direction of the reflected ray can be approximately calculated and is denoted by the unit vector $\hat{\mathcal{R}}'$ (see in Fig. 7). Finally, $\hat{\mathcal{R}}'$ is substituted into Eq. (19) to compute the unit normal vectors $\hat{n}$.

In practice, either the ophthalmologist, or optometrist, cannot perfectly align the human cornea with the corneal topographer axis; therefore, the cornea vertex does not coincide with the Origin of coordinates or designed position.

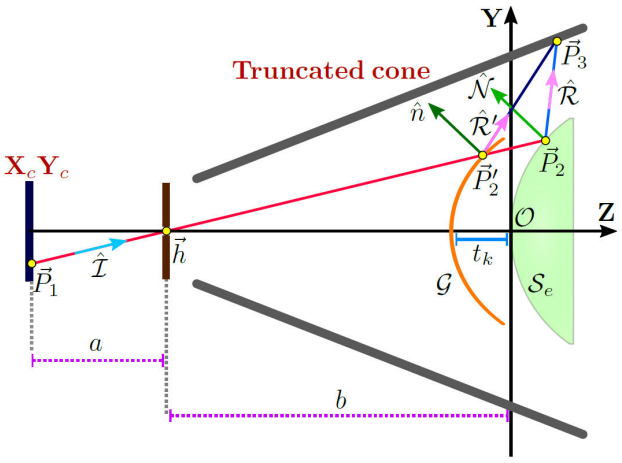

FIGURE 7. Representation of surface $\mathcal{G}(x, y)$, positioned at t_k, used for computing the normal vectors.

this drawback, in order to enhance the calculation of the slopes, the surface $\mathcal{G}$ is positioned at several positions along the **Z**-axis, denoted by t_k, until the closest surface to the test surface is obtained. The position of $\mathcal{G}$ is in the interval denoted by $(t_1, t_2, \ldots, t_k, \ldots, t_K)$, taking the center of the interval as the position of the surface considered to design the null-screen. This implies that a set of k surfaces $\mathcal{G}(x, y)$ are positioned along the **Z**-axis for obtaining a normal vector field for each surface. In addition, we define $S_x{=}(-n_x/n_z)$ and $S_y{=}(-n_y/n_z)$ as the slopes to the surface under study. The value of the sagitta for the test surface is obtained using the following line integral

$$z = t_k + \int \left(S_x dx + S_y dy\right), \tag{20}$$

as we mentioned before, t_k is the position of $\mathcal{G}$ along the **Z**-axis. We use the trapezoidal rule [28] for calculating the definite integral in Eq. (20). As a result, a point cloud $\{x, y, z\}$ is recovered for each surface positioned at t_k. Furthermore, we propose that each surface under test can be represented by a linear combination $\Psi(x, y)$ of polynomial functions $\psi_i(x, y)$ as follows

$$\Psi(x, y) = \sum_{i=1}^{N} B_i \psi_i(x, y), \tag{21}$$

where $\psi_i(x, y)$ will be taken as the Taylor monomials and $N = 55$. The partial derivatives of $\Psi(x, y)$, with respect to the Cartesian coordinates x and y, are fitted to the slopes S_x and S_y using a modal reconstruction as described in Ref. [29]. As a result, the values of the coefficients B_i are obtained. In addition, the normal vector to $\Psi(x, y)$ can be calculated as

$$\hat{\mathcal{U}} = \left(\Psi_x, \Psi_y, -1\right) / \sqrt{\Psi_x^2 + \Psi_y^2 + 1}, \tag{22}$$

where Ψ_x and Ψ_x are the partial derivatives with respect to the Cartesian coordinates x and y, respectively. For determining how close the k-th reconstructed surface is to the actual surface, we compare the normal vectors $\hat{n}$ (see Eq. 19) with $\hat{\mathcal{U}}$ (see Eq. 22), *i.e.*, we calculate the standard deviation of the set of differences denoted by $\delta_k{=}\{\parallel \hat{\mathcal{U}} - \hat{u} \parallel\}_k$, where the subscript k refers to the k-th reconstructed surface. Therefore, a collection of k values for δ_k is obtained, whereas the surface closest to the actual one corresponds to the minimum $\Delta_{k'}$ of these values. This surface is denoted by $\Psi_{k'}$, and its vertex position is at $t_{k'}$. Ideally, $\Delta_{k'}$ should be zero, *i.e.*, the unit vectors $\hat{n}$ and $\hat{\mathcal{U}}$ should coincide. This is because the reconstructed surface must satisfy the reflection law and the normal vectors to the surface must be equal, it does not matter whether they were calculated using the directions of the rays (see Eq. (19)) or the gradient [see Eq. (22)]. In order to refine the result, a new interval can be defined as $(t_{k'} - \Delta t, t_{k'} + \Delta t)$ and partitioned into K' equal parts, where $\Delta t = t_2 - t_1$. The algorithm ends when the stopping criterion is satisfied, *i.e.*, $\Delta_{k'} \leq TOL$, where $TOL = 2 \times 10^{-7}$. Figure 8 shows a

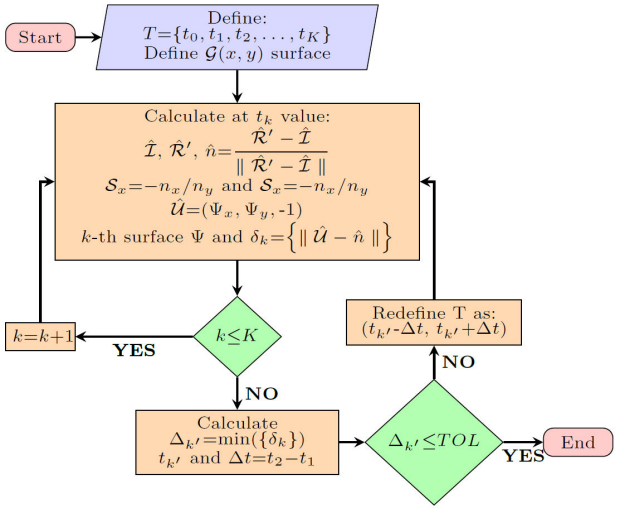

FIGURE 8. Flowchart illustrating the reconstruction algorithm.

flowchart of the reconstruction algorithm. A more detailed exposition about the reconstruction algorithm can be found in Ref. [23].

4.2. Calculation of the axial and tangential maps

Two quantities widely used to characterize the anterior corneal surface are the axial (sagittal) and meridional (tangential) curvatures denoted by $\mathcal{K}_a$ and $\mathcal{K}_m$, respectively. Both quantities are calculated along a corneal meridian, as will be discussed below.

In order to obtain the curvatures $\mathcal{K}_a$ and $\mathcal{K}_m$, we use the analytical representation for the reconstructed surface, $\Psi(x, y)$, given by Eq. (21). We set the first three coefficients to zero, as they do not affect the surface shape. B_1 displaces the surface along the **Z**-axis. B_2 and B_3 tilt the surface with respect to the **X** and **Y** axes, respectively. The polynomial function $\Psi(x, y)$ is evaluated in a radial domain as schematized in Fig. 9a) and 9b). Along a meridian defined by the angle θ, the sagitta of the surface is denoted by the function $\mathcal{F}(\rho)$, as illustrated in Fig. 9c).

The curve $(\rho, \mathcal{F}(\rho))$ can be described as a polynomial function in the following form

$$\mathcal{F}(\rho) = \sum_{i=1}^{8} c_i \rho^i. \tag{23}$$

To obtain the coefficients c_i of the polynomial function that best fits the data points $(\rho, \mathcal{F}(\rho))$, we use the instruction

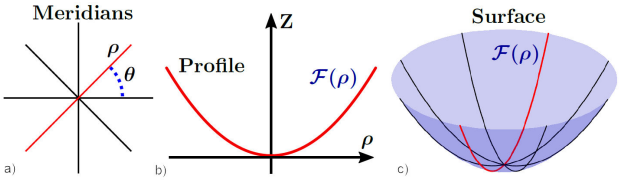

FIGURE 9. a) Radial domain. b) Surface represented by $\Psi(x, y)$. c) Sagitta along a meridian defined by the angle θ.

polyfit which is implemented in MATLAB toolbox and is based on the least squares method [30]. Once the coefficients c_i are determined, the axial and meridional curvatures along the meridian defined by θ can be calculated as [2, 7, 31]

$$\mathcal{K}_a = \frac{\mathcal{F}_\rho}{\rho\left(1+\mathcal{F}_\rho^2\right)^{\frac{1}{2}}}, \quad \mathcal{K}_m = \frac{\mathcal{F}_{\rho\rho}}{\left(1+\mathcal{F}_\rho^2\right)^{\frac{3}{2}}}, \tag{24}$$

where $\mathcal{F}_\rho$ and $\mathcal{F}_{\rho\rho}$ denote the first and second derivatives of $\mathcal{F}$ with respect to ρ. For the purpose of obtaining the curvature values on the reconstructed surface, the calculation of $\mathcal{K}_a$ and $\mathcal{K}_m$ must be done for all meridians of a radial domain previously defined. From the values for $\mathcal{K}_a$ and $\mathcal{K}_m$, it is possible to obtain the axial (sagittal) and meridional (tangential) powers denoted by $\mathcal{P}_a$ and $\mathcal{P}_m$, respectively. The optical powers can be calculated as follows

$$\mathcal{P}_a = (n_c - n')\,\mathcal{K}_a, \quad \mathcal{P}_m = (n_c - n')\,\mathcal{K}_m, \tag{25}$$

where n_c is the refractive of the cornea and n' is the refractive index of the surrounding medium. In practice, n_c and n' are considered as the keratometric refractive index ($n_c = 1.3375$) and the air refractive index ($n' \approx 1$), respectively. In addition, in Eq. (25) the units of the optical powers must be inverse meters (m^{-1}), also known as diopters (D).

The spherical surface used to design the target inside the truncated cone (see Fig. 4), exhibits constant curvatures $\mathcal{K}_m$ and $\mathcal{K}_a$, both equal to $1000/7.8$ m^{-1}. Therefore, the corresponding power distributions $\mathcal{P}_m$ and $\mathcal{P}_a$ remain constant at 43.26 D, as illustrated in Figs. 10a) and 10b), respectively. In contrast, Figs. 10c) and 10d) depict the power distributions $\mathcal{P}_m$ and $\mathcal{P}_a$ for the biconical surface under test, which is defined by Eq. (12). The contour maps of $\mathcal{P}_m$ and $\mathcal{P}_a$ form a pattern classically known as bow-tie or hourglass [21]. The presence of the bow-tie in both power maps indicates that the corneal surface will produce the astigmatism aberration. The orientation of the bow-tie coincides with the steeper meridian

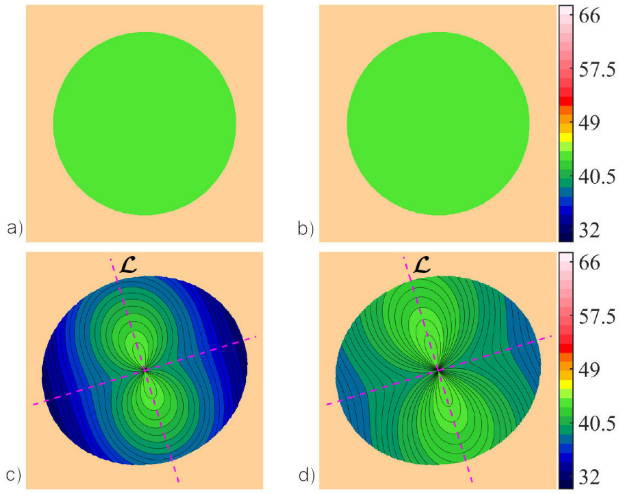

FIGURE 10. Spherical surface: a) Meridional power $\mathcal{P}_m$ and b) Axial power $\mathcal{P}_a$. Biconical surface under test: c) Meridional power $\mathcal{P}_m$ and d) Axial power $\mathcal{P}_a$.

denoted by $\mathcal{L}$ in Figs. 10c) and 10d), in this case the astigmatism is classified as with-the-rule astigmatism. But if the steeper meridian is closer to the horizontal axis, the astigmatism is called against-the-rule astigmatism [1].

5. Results of numerical simulations

Throughout this section, we recover the corneal topographies that should be generated by each image affected by distortion shown in Fig. 5b) and Figs. 6a) - 6f). Applying the reconstruction algorithm described in Sec. 4, we retrieve in each case the shape of the surface under test which is represented as a height map. In addition, in each case, a difference map is used to show the deviations between the reconstructed surface and the ideal surface, which is represented by Eq. (12) and Table III. Furthermore, we fit Eq. (12) to the Cartesian coordinates (x, y, z) corresponding to the recovered surface, to obtain the parameters of the biconical surface that best fits the point cloud (x, y, z), with the aim of carrying out a comparison with the ideal values listed in Table III.

Whenever the reconstruction algorithm is applied, using each image affected by distortion, a polynomial function $\Psi(x, y)$ given by Eq. (21) is obtained for each recovered surface. Using $\Psi(x, y)$, the axial and tangential powers are calculated in accordance with the process described in Sec. 4.2, and both powers are shown in contour maps.

As mentioned before, from the change in image size due to distortion aberration, the position of the points (x_c, y_c) on the detection plane deviates from the actual position. As a result, the unit vector $\hat{\mathcal{I}}$ given by Eq. (3) changes its direction; therefore, the normal vectors $\hat{n}$ calculated using Eq. (19) also undergo changes in direction. The above discussion suggests that the reconstruction algorithm would recover a surface at an incorrect position along the **Z**-axis or with a shape deviating from the actual surface.

5.1. Retrieving the corneal topography

Applying the reconstruction algorithm to each image affected by distortion, we obtain the height, and the difference and curvature maps, which are shown in rows in Fig. 11. The value for the coefficient σ, increasing from top to bottom, appears at the bottom of Figs. 11a) - 11g).

In Fig. 11, all contour maps are shown in a square domain $[-6.1$ mm, 6.1 mm$]\times[-6.1$ mm, 6.1 mm$]$. We must note that the maps plotted in Fig. 11d) correspond to the synthetic image without distortion ($\sigma = 0$) shown in Fig. 5b). Furthermore, by fitting Eq. (12) to the recovered surface using the least squares method implemented in the MATLAB toolbox, we obtain the values for the radii of curvature (r_x and r_x), the conic constants (k_x and k_y) and the rotation angle (α). These values are listed in Table VI.

Once the reconstruction algorithm was applied to all cases, the surfaces were recovered close to the Origin of coordinates $\mathcal{O}$. In order words, the closest surface to the actual surface is obtained when the surface $\mathcal{G}$ is positioned very close to $\mathcal{O}$, as depicted in Fig.7. This happens because the distorted images are very similar to the image without distortion in the central region. The amount of distortion is proportional to the image size, as can be seen from the second term on the right side of Eq. (18a) and Eq. (18b). The vertex positions of the recovered surfaces along the **Z**-axis, denoted by t_k, are listed in Table VI.

The conical profiles along the principal axes of the retrieved surface are plotted in Figs. 12a) and 12b), showing the effects of distortion aberration at the periphery of the recovered surface. As the distortion coefficient increases and

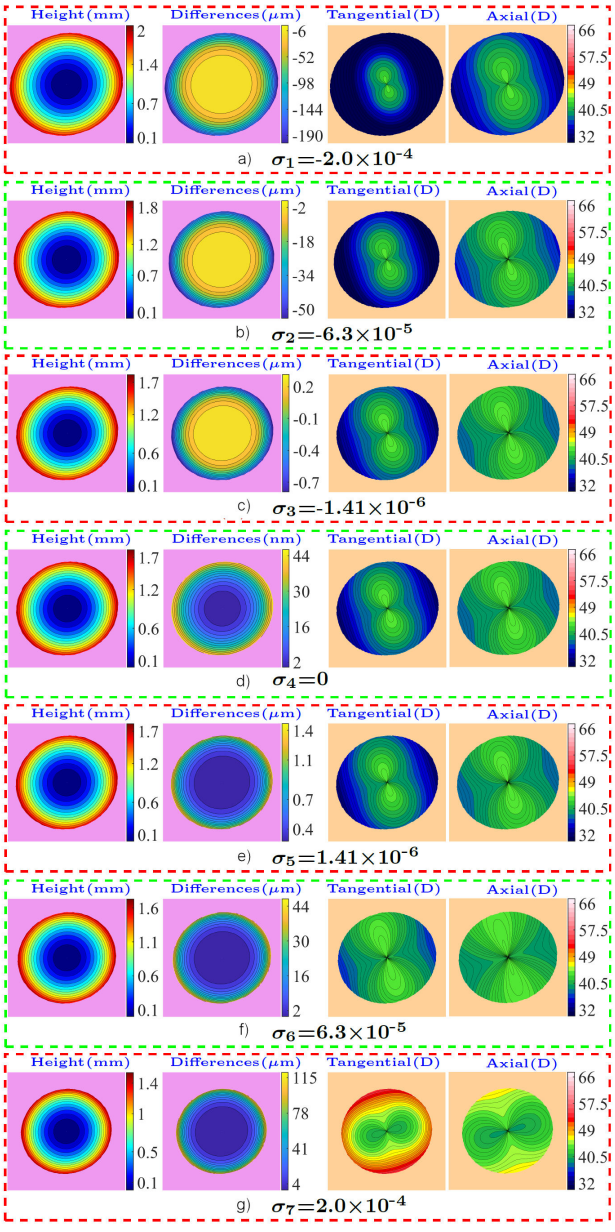

FIGURE 11. Heights, differences and diopter powers recovered from images affected by different degrees of distortion: a) $\sigma_1 = -2.0 \times 10^{-4}$, b) $\sigma_2 = -6.3 \times 10^{-5}$, c) $\sigma_3 = -1.41 \times 10^{-6}$, d) $\sigma_4 = 0$, e) $\sigma_5 = 1.41 \times 10^{-6}$, (f) $\sigma_6 = 6.3 \times 10^{-5}$, g) $\sigma_7 = 2.0 \times 10^{-4}$.

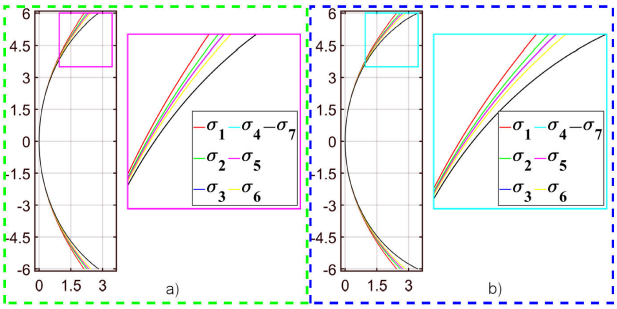

FIGURE 12. Conical profiles along a) the x-axis and b) the y-axis of the retrieved surface.

TABLE VI. Parameters corresponding to the biconical surface that best fits the recovered surface.

Fig.	$[r_x, r_y]$ (mm)	$[k_x, k_y]$	α (°)	t_k (μm)
11a)	[8.350, 7.661]	[-1.106, -0.774]	16.999	-3.636
11b)	[8.344, 7.636]	[-0.658, -0.425]	16.999	-1.188
11c)	[8.349, 7.629]	[-0.435, -0.254]	17.000	-0.311
11d)	[8.349, 7.629]	[-0.429, -0.249]	17.000	-0.293
11e)	[8.350, 7.629]	[-0.424, -0.245]	17.000	0.274
11f)	[8.360, 7.627]	[-0.184, -0.062]	16.999	0.408
11g)	[8.415, 7.641]	[0.435, 0.400]	16.999	1.757

transitions from negative to positive, the periphery of the profiles moves closer to the horizontal axis, as shown in Fig. 12. According on the values of the conic constants k_x and k_y, the profiles can be classified as follows: hyperboloid ($k_{x,y}<-1$), prolate spheroid or ellipsoid ($-1<k_{x,y}<0$), and oblate spheroid ($0<k_{x,y}$) [32]. The profiles corresponding to σ_3, σ_4, and σ_5 are overlapped.

The values for the radii of curvature r_x and r_y tabulated in Table VI, corresponding to the biconical surface that best fits to the reconstructed surface, are close to the actual values listed in Table III. The percentage errors $\mathcal{E}_{r_x}$ and $\mathcal{E}_{r_y}$ associated with r_x and r_y are plotted in Fig. 13a) and are less than 0.8%. Nevertheless, in some cases, the percentage errors associated with the conic constants k_x and k_y become greater than 200%, as shown in Fig. 13b). As a consequence the periphery of the recovered surface deviates from the actual surface, in accordance with the difference maps shown in Figs. 11a)-g) and the profiles plotted in Fig. 12.

If the shape of the reconstructed surface is used in the adaptation of contact lenses, the corneal topographer may suggest a base curvature for the contact lens that does not fit properly to the anterior corneal surface. Furthermore, from Table VII, k_x and k_y become increasingly positive as the distortion coefficient increases. We can note that the values for the conic constants k_x and k_y, recovered using Fig. 11g) (see the last row of Table VI), have suffered a sign change. As a consequence, from the powers maps shown in Fig. 11g), the bow tie apparently suffers a rotation of 90 degree, *i.e.*, if the camera distortion is not corrected, the corneal astigmtism

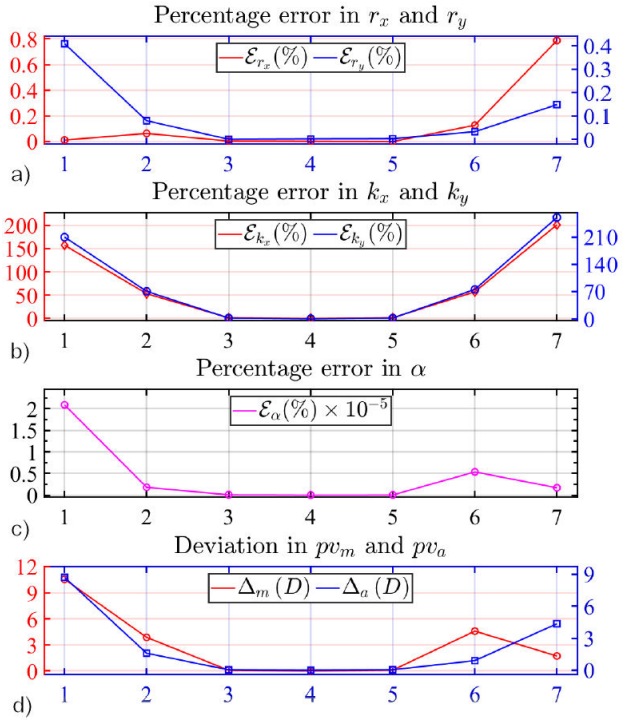

FIGURE 13. Percentage errors in: a) radii of curvature r_x and r_y, b) conic constants k_x and k_y and c) the rotation angle α. d) Deviations of pv_m and pv_a with respect to the ideal values.

may be erroneously classified as against-the-rule astigmatism.

Another recovered parameter from the fitting is the angle of rotation corresponding to each reconstructed surface. Fig. 13c) shows the graph for the percentage errors associated with the angles of rotation α. The percentage errors, represented by $\mathcal{E}_\alpha$, are less than 3×10^{-5} %, *i.e.*, in all cases the angle α is very close to the true value. The latter can be attributed to the proposed type of distortion aberration, since it only affects the image in the radial direction. Additionally, the vertex of the surface under test was proposed to be aligned with the corneal topographer axis. The difference between the recovered surface and the actual surface is defined as

$$\Delta S = \text{ideal biconical surface} - \text{recovered surface}. \quad (26)$$

The peak-to-valley (pv) and root-mean-square (rms) errors associated with ΔS are given by

$$pv = \mathbf{max}(\Delta S) - \mathbf{min}(\Delta S), \quad (27a)$$

$$rms = \sqrt{\frac{\sum_i^N (\overline{\Delta S} - \Delta S)^2}{N}}, \quad (27b)$$

where **max**() and **min**() calculate the maximum and minimum of the values set in the parentheses, respectively. N represents the number of points that make up the recovered surface, and $\overline{\Delta S}$ denotes the mean value of the differences

TABLE VII. Parameters calculated from the difference and power maps shown in Figs. 11a)-11f).

Fig.	pv	rms	pv_m	pv_s
11a)	206.65 μm	48.24 μm	23.06 D	15.64 D
11b)	55.46 μm	12.92 μm	16.37D	8.52D
11c)	1.10 μm	0.254 μm	12.590 D	6.97 D
11d)	46.32 nm	12.86 nm	12.49 D	6.93 D
11e)	1.19 μm	0.27 μm	12.40 D	6.89 D
11f)	47.30 μm	10.97 μm	7.917 D	6.03 D
11g)	122.50 μm	28.27 μm	14.23 D	11.29 D

ΔS. The pv and rms errors are tabulated in Table VII. pv and rms can be up to a few hundred microns, however, when the distortion coefficient is zero [Fig. 11d)], then pv and rms are of the order of some nanometers. The above highlights the importance of minimizing distortion effects in the image to achieve reliable and consistent corneal topography measurements.

Additionally, we define the quantities pv_m and pv_a as the peak-to-valley of the meridional power and the axial power, respectively. They can be calculated as follows:

$$pv_m = \mathbf{max}(\mathcal{K}_m) - \mathbf{min}(\mathcal{K}_m), \tag{28a}$$

$$pv_m = \mathbf{max}(\mathcal{K}_a) - \mathbf{min}(\mathcal{K}_a). \tag{28b}$$

The recovered values of pv_m and pv_a are listed in Table VII. The ideal values are 12.507 D and 6.938 D, correspondingly. The latter values were calculated from the power maps shown in Fig. 10a) and 10b). The discrepancies between pv_m and pv_a and their actual values are denoted by $\Delta_m = 12.507 - pv_m$ and $\Delta_a = 6.938 - pv_a$, respectively. Figure 13d) shows the plots corresponding to Δ_m and Δ_a, it is clear that the deviations increase proportionally to the magnitude of the distortion coefficients.

As mentioned before, laser ablation technique can be used to reshape the anterior corneal surface for treating refractive errors such as myopia, hyperopia and astigmatism. The ablation laser uses the corneal topography to obtain the optimal corneal curvature to reduce the refractive errors [4–6]. However, if the corneal topographer uses images affected by distortion aberration, the sagitta and the diopter power deviates from the true values. As a consequence, the ablation laser could remove undesired material from regions of the anterior corneal surface, resulting in an overcorrection or undercorrection of the refractive errors. From the results obtained throughout this section, the importance of carrying out a calibration procedure of the distortion aberration, associated with the optical system of the corneal topographer camera, is highlighted.

6. Conclusions

Throughout this paper, we have presented an analysis of the effects on corneal topography measurements when the corneal topographer camera is affected by radial distortion aberration. To carry out the analysis we used synthetic images calculated in numerical form and distorted using Seidel's aberrations. These images theoretically correspond to the images produced by the reflected light on a biconical surface rotated about the **Z**-axis, which is considered as the corneal surface under test. The corneal topographer in which the calculations are based consists essentially of a smartphone and a truncated cone, while the target inside the cone was designed using the Null Screen Method.

Several degrees of distortion, ranging from negative to positive, were tested on the synthetic images, resulting in changes in size. For example, pincushion and barrel distortions cause image expansion and contraction, respectively. While qualitative inspection of the distorted images might initially suggest that the surface under test is displaced from the ideal position, or that its radius of curvature deviates from the average human cornea, once the reconstruction algorithm was applied, the results showed that the surface retrieved by the algorithm was located very close to the true position of the vertex. For the cases considered in this study, although the radii of curvature exhibited minimal deviations (less than 0.8%), the conic constants displayed significant errors (up to 200%) due to the discrepancies between the reconstructed surface and the ideal surface particularly in the periphery. If the reconstructed surface is used in the adaptation of contact lenses, this could lead to inaccurate contact lens fitting, as the base surface would not be suitable. Moreover, in order to reshape the anterior corneal surface via laser ablation, it is essential to conduct a preoperative assessment of the patient's corneal topography. However, as we have shown, if the corneal topographer camera introduces distortion aberration, then the corneal topography deviates from the true values. As a consequence, the ablation laser may remove material from undesired regions of the anterior corneal surface, which could result in overcorrection or undercorrection of the refractive errors. Therefore, the results presented in this paper emphasize the critical importance of calibrating distortion aberration in corneal topographer cameras to ensure accurate and reliable results in the assessment of human corneal topography.

Acknowledgments

The authors acknowledge the economic support received by CONAHCYT for the postdoctoral fellowship to Oliver Huerta-Carranza (CVU 710606). In addition, the authors received financing by DGAPA-UNAM through the projects IT103623 and IT104525.

Disclosures

The authors declare no conflicts of interest.

1. D. A. Atchison and G. Smith, Refracting Components: Cornea and Lens, in Optics of the human eye (Butterworth-Heinemann, 2000), pp. 15-41.
2. M. Kaschke, K. H. Donnerhacke, and M. S. Rill, Optical Devices in Ophthalmology and Optometry. Technology, Design Principles, and Clinical Applications, (Wiley-VCH, 2014).
3. S. L. Hill, Non-Surgical Treatment of Keratoconus Using Contact Lenses, in Keratoconus & keratoectasia: prevention, diagnosis, and treatment, M. Wang and T. S. Swartz, Eds., (Slack Incorporated 2010), pp 119-132.
4. D. Gatinel, T. Hoang-Xuan and D. T. Azar, Three-dimensional representation and qualitative comparisons of the amount of tissue ablation to treat mixed and compound astigmatism, *J Cataract Refract Surg* **28** (2002) 2026.
5. T. Sakimoto, M. I. Rosenblatt and D. T. Azar, Laser eye surgery for refractive errors, *Lancent* **367** (2006) 1432.
6. S. C. Ipek and C. A. Utine, Topography-Guided Excimer Laser Ablation in Refractive Surgery, *Frontiers in Ophthalmology*, **4** (2024) 1.
7. Y. MejÃa-Barbosa and D. Malacara-Hernández, A Review of Methods for Measuring Corneal Topography, *Optometry and Vision Science* **78** (2001) 240.
8. J. M. Jalife-Chavira, G. Trujillo-Schiaffino, P. G. Mendoza-Villegas, D. P. Salas-Peimbert, M. Anguiano-Morales and L. F. Corral-MartÃnez, Optical methods for measuring corneal topography: A review, *Opt. Pura Apl*. **52** (2019) 1.
9. N. T. Al-Sharify, S. M. Ahmed, H. Y. Nser, O. H. See, Z.T. Al-Sharify, N. H. Ghaeb, L. Y. Weng, Corneal topography, an overview of its devices and systems-A review, *AIP Conf. Proc.* **090041** (2023) 2787.
10. A. K. Ghatak and K. Tahyagarajan, Geometrical theory of third-order aberrations, in Contemporary Optics (Plenum, 1978), pp. 31-70.
11. S. Lee, B. Kim, J. Lee, and J. Sasian, Accurate determination of distortion for smartphone cameras, *Appl. Opt*. **53** (2014) H1.
12. Z. Tang, R. Grompone von Gioi, P. Monasse and J.-M. Morel, A Precision Analysis of Camera Distortion Models, *IEEE Trans. Image Process* **26** (2017) 2694.
13. M. Campos-GarcÃa, D. Aguirre-Aguirre, V. I. Moreno-Oliva, O. Huerta-Carranza, and V. Armengol-Cruz, Measurement and correction of misalignments in corneal topography using the null-screen method, *OSA Continuum* **4** (2021) 158.
14. O. Huerta-Carranza, M. Campos-García, V. I. Moreno-Oliva, D. Aguirre-Aguirre, and J. S. Pérez-Lomelí, Smartphone-based corneal topography with null-screens, *Appl. Opt*. **61** (2022) 1381.
15. M. Campos-García, O. Huerta-Carranza, V. I. Moreno-Oliva, D. Aguirre-Aguirre, and L. A. Pantoja-Arredondo, Corneal topography using a smartphone-based corneal topographer considering a biconical model for the corneal surface, *Opt. Continuum* **3** (2024) 751.
16. S. A. Klein, Axial Curvature and the Skew Ray Error in Corneal Topography, *Optometry and Vision Science* **74** (1997) 931.
17. Daniel Gomez-Tejada, Daniel Malacara Hernández, A proposal to eliminate the skew ray error in corneal topography using Placido disks images *Proc. SPIE* **11102** (2019) 1110206.
18. D. Gómez-Tejada, Z. Malacara-Hernández, D. Malacara-Doblado, and D. Malacara-Hernández, Zonal integration of circular Hartmann and Placido patterns with non-rotationally symmetric aberrations, *J. Opt. Soc. Am. A* **37** (2020) 1381.
19. O. Huerta-Carranza, M. Campos-García, L. A. Pantoja-Arredondo, F. Granados-Agustín, Effect of the skew ray error on corneal topography using a cone topographer, *Proc. SPIE* **13021** (2024) 130210A.
20. R. Kingslake and R. B. Johnson, Aberration Theory, in Lens Design Fundamentals (SPIE, 2010), pp. 101-135.
21. M. Wang, *Corneal Topography: A Guide for Clinical Application in Wavefront Era*, 2nd ed. (Slack Incorporated 2011).
22. J. J. Snellenburg, B. Braaf, E. A. Hermans, R. G.L. van der Heijde, and V. A. D. P. Sicam, Forward ray tracing for image projection prediction and surface reconstruction in the evaluation of corneal topography systems, *Opt. Express* **18** (2010) 19324.
23. O. Huerta-Carranza, M. Avendaño-Alejo, and R. DÃaz-Uribe, Null screens to evaluate the shape of freeform surfaces: progressive addition lenses, *Opt. Express* **29** (2021) 27921.
24. A. Fitzgibbon, M. Pilu and R. B. Fisher, Direct least square fitting of ellipses, *IEEE Trans. Pattern Anal. Mach. Intell*. **21** (1999) 476.
25. P. Sturm, Pinhole Camera Model, In *Computer Vision*, K. Ikeuchi, Ed., (Springer, Boston) (2014) pp 610-613.
26. J. Weng, P. Cohen and M. Herniou, Calibration of stereo cameras using a non-linear distortion model, in *Proceedings of the 10th International Conference on Pattern Recognition* (Atlantic City, NJ), **1** (1990) 246.
27. Z. Zhang, A flexible new technique for camera calibration, *IEEE Transactions on pattern analysis and machine intelligence*, **22** (2000) 1330.
28. W. H. Press, Integration of Functions, in Numerical Recipes: The Art of Scientific Computing (Cambridge, 2007), pp. 155-200.
29. J. Ye, L. Chen, X. Li, Q. Yuan and Z. Gao, Review of optical freeform surface representation technique and its application, *Opt. Eng*. **56** (2017) 110901.
30. R. S. Esfandiari, Curve Fitting and Interpolation, in Numerical methods for engineers and scientists using MATLAB (CRC Press, 2013), pp 161-248.
31. A. Estrada-Molina, M. Campos-García, and R. Díaz-Uribe, Sagittal and meridional radii of curvature for a surface with symmetry of revolution by using a null-screen testing method, *Appl. Opt*. **52** (2013) 625.
32. R. E. Fischer, B. Tadic-Galeb and P. R. Yoder, Spherical and Aspheric Surfaces, in Optical System Design (SPIE, 2010), pp. 115-127.